

A comparison between grid and particle methods on the small-scale dynamo in magnetized supersonic turbulence

Terrence S. Tricco,^{1,2,3★} Daniel J. Price^{3★} and Christoph Federrath^{3,4★}

¹Canadian Institute for Theoretical Astrophysics, University of Toronto, 60 St. George Street, Toronto, ON M5S 3H8, Canada

²School of Physics, University of Exeter, Stocker Road, Exeter EX4 4QL, UK

³Monash Centre for Astrophysics, School of Physics and Astronomy, Monash University, Clayton, VIC 3800, Australia

⁴Research School of Astronomy and Astrophysics, Australian National University, Canberra, ACT 2611, Australia

Accepted 2016 May 26. Received 2016 May 26; in original form 2015 September 7

ABSTRACT

We perform a comparison between the smoothed particle magnetohydrodynamics (SPMHD) code, PHANTOM, and the Eulerian grid-based code, FLASH, on the small-scale turbulent dynamo in driven, Mach 10 turbulence. We show, for the first time, that the exponential growth and saturation of an initially weak magnetic field via the small-scale dynamo can be successfully reproduced with SPMHD. The two codes agree on the behaviour of the magnetic energy spectra, the saturation level of magnetic energy, and the distribution of magnetic field strengths during the growth and saturation phases. The main difference is that the dynamo growth rate, and its dependence on resolution, differs between the codes, caused by differences in the numerical dissipation and shock capturing schemes leading to differences in the effective Prandtl number in PHANTOM and FLASH.

Key words: magnetic fields – MHD – shock waves – turbulence – methods: numerical – ISM: magnetic fields.

1 INTRODUCTION

Supersonic turbulence regulates star formation (Mac Low & Klessen 2004; McKee & Ostriker 2007; Hennebelle & Falgarone 2012; Padoan et al. 2014), producing the dense filaments that permeate molecular clouds along which dense cores and protostars form (e.g. Larson 1981; Hartmann 2002; Elmegreen & Scalo 2004; Hatchell et al. 2005; André et al. 2010; Peretto et al. 2012; Federrath 2016; Hacar et al. 2016; Kainulainen et al. 2016). That molecular clouds are magnetized cannot be ignored. Magnetic fields are no longer thought to prevent gravitational collapse altogether, but may still determine the rate and efficiency of star formation, even with weak magnetic fields, via super-Alfvénic turbulence (Nakamura & Li 2008; Price & Bate 2008, 2009; Lunttila et al. 2009; Padoan & Nordlund 2011; Federrath & Klessen 2012; Federrath 2015). Therefore, it is vital to understand processes which determine the magnetic field strength inside molecular clouds. These processes involve highly non-linear dynamics making analytic study difficult (though see Sridhar & Goldreich 1994; Goldreich & Sridhar 1995), while observations of magnetic fields in molecular clouds are time consuming and only yield field directions in the plane of the sky and magnitudes along the line of sight (e.g. Crutcher 1999, 2012; Bourke et al. 2001; Heiles & Troland 2005; Troland & Crutcher 2008; Crutcher et al. 2010). Numerical simulations can comple-

ment analytics and observations, and it is important to compare results from different codes to establish the conditions under which those results are representative of the physical processes involved. In this work, we focus on the small-scale turbulent dynamo as a mechanism for magnetic field amplification in molecular clouds, comparing calculations using smoothed particle magnetohydrodynamics (SPMHD) with those using grid-based methods.

1.1 Small-scale turbulent dynamo

The small-scale dynamo grows magnetic fields in a turbulent environment by the conversion of kinetic energy into magnetic energy. Operating near the dissipation scale, it is there that the smallest motions can efficiently grow the magnetic field through rapid winding and twisting of the magnetic field lines, with the magnetic energy growing exponentially via a reverse cascade of energy from small to large scales (see review by Brandenburg & Subramanian 2005).

The exponential growth rate is determined primarily by the physical viscosity and magnetic resistivity of the plasma, which can be expressed as dimensionless numbers: the kinematic Reynolds number ($Re = VL/\nu$, where V is the velocity, L is the characteristic length, and ν is the kinetic dissipation), the magnetic Reynolds number ($Rm = VL/\eta$, where η is the resistive dissipation), and the ratio of the two, the ‘magnetic Prandtl number’, $Pm = Rm/Re$ (Schekochihin et al. 2004a; Brandenburg & Subramanian 2005; Schober et al. 2012a,b; Bovino, Schleicher & Schober 2013; Federrath et al. 2014). Using a large set of numerical simulations, Federrath et al. (2011) found that the dynamo growth rate is also

* E-mail: tricco@cita.utoronto.ca (TST); daniel.price@monash.edu (DJP); christoph.federrath@anu.edu.au (CF)

dependent upon the compressibility of the plasma, parametrized by the turbulent Mach number, and is more efficient for turbulence driven by solenoidal (rotational) flows rather than compression.

The magnetic field will saturate first at the dissipation scale, after which the dynamo enters a slow linear or quadratic magnetic energy growth phase (Cho et al. 2009; Schleicher et al. 2013). This occurs due to the back-reaction of the Lorentz force on the turbulent flow as it begins to resist the winding of the magnetic field (Schekochihin et al. 2002; Schober et al. 2015). The magnetic field on larger spatial scales will continue to slowly grow through reverse cascade of magnetic energy. Thus the small-scale dynamo can be considered as progressing through three distinct phases: (i) the exponential growth phase; (ii) the slow linear or quadratic growth phase once the magnetic energy is saturated at the dissipation scale; and (iii) the saturation phase once the magnetic field has saturated on all spatial scales.

1.2 Previous turbulence comparisons

Simulating magnetized, supersonic turbulence is challenging due to the range of flow conditions present and the need to uphold the divergence-free constraint of the magnetic field. Comparing results between different numerical methods is the best way to be confident in their results, and there have been several major code comparison projects related to supersonic turbulence. Tasker et al. (2008) compared two grid codes (ENZO, FLASH) and two smoothed particle hydrodynamics (SPH) codes (GADGET2, HYDRA) on simple test problems involving strong hydrodynamic shocks, finding comparable results when the number of particles were roughly equal to the number of grid cells. Kitsionas et al. (2009) studied decaying, supersonic, hydrodynamic (non-magnetized) turbulence, comparing four grid codes (ENZO, FLASH, TVD, ZEUS) and three SPH codes (GADGET, PHANTOM, VINE). They found similar velocity power spectra and density probability distribution functions (PDFs) when the number of resolution elements were comparable, though the particle codes were found to be more dissipative. Kritsuk et al. (2011b) compared decaying, supersonic turbulence with magnetohydrodynamics (MHD) using nine different grid codes: ENZO, FLASH, KT-MHD, LL-MHD, PLUTO, PPML, RAMSES, STAGGER, and ZEUS. They found that all methods produced physically consistent results, with the quality of results improved with higher order numerical solvers, and by exactly rather than approximately maintaining the divergence-free constraint on the magnetic field.

A key limitation of both the Kitsionas et al. (2009) and Kritsuk et al. (2011b) comparisons is that they studied decaying turbulence. Interpolating the initial conditions obtained by driving the turbulence in one code introduced discrepancies between codes before the numerical experiments even started. Those discrepancies in the initial conditions were most severe between grid and particle methods, but also for different grid discretizations (e.g. staggered versus unstaggered meshes), and is problematic in the MHD case since one must enforce $\nabla \cdot \mathbf{B} = 0$. Furthermore, it is difficult to obtain a statistically significant sample of simulation snapshots in the absence of a statistical steady-state, given that supersonic turbulence decays within a few crossing times. This limitation means that intermittent, intrinsic fluctuations of the turbulence largely exceeded systematic differences in the numerical schemes, which we want to quantify.

Price & Federrath (2010, hereafter PF10) addressed these issues in a hydrodynamic comparison by using driven instead of decaying turbulence, allowing time-averaged statistical comparisons. They compared two codes: the grid code, FLASH, and the SPH code, PHANTOM. The calculations started from a well-defined initial state

of uniform density gas at rest, and both codes used exactly the same turbulence driving routine and force sequence to prevent any bias from different implementations. They found similar resolution requirements to previous studies, but that grid-based methods were better at resolving volumetric statistics at a given resolution, while SPH better sampled density-weighted quantities. However, this comparison was limited to hydrodynamic turbulence.

Recently, Tricco & Price (2012) developed a new divergence cleaning method for SPMHD that maintains $\nabla \cdot \mathbf{B} = 0$ to sufficient accuracy for a wide range of problems, such as the simulation of jets and outflows during protostar formation (Price, Tricco & Bate 2012; Bate, Tricco & Price 2014; Lewis, Bate & Price 2015; Wurster, Price & Bate 2016). The best prior approach to maintain the divergence-free constraint was the Euler potentials, defining $\mathbf{B} = \nabla\alpha \times \nabla\beta$ (Price & Bate 2007; Rosswog & Price 2007). However, this excludes dynamo processes by construction because the Euler potentials cannot represent and follow wound-up magnetic field structures (Price & Bate 2008; Brandenburg 2010; Price 2012). By directly evolving the magnetic field and enforcing the divergence-free constraint with the constrained hyperbolic divergence cleaning method (Tricco & Price 2012), it is now possible to simulate magnetohydrodynamic turbulence and MHD dynamos with SPMHD. Furthermore, Tricco & Price (2013) improved the magnetic shock-capturing algorithm, particularly when dealing with weak magnetic fields in strong shocks.

1.3 Outline

This paper presents a code comparison on the small-scale dynamo amplification of a weak magnetic field from driven, supersonic turbulence. For our comparison, we use the same hydrodynamic codes, driving routine, and Mach number as the PF10 comparison, so that any differences arise only from the MHD implementation. We investigate the three phases of small-scale dynamo amplification: exponential growth of magnetic energy, slow linear or quadratic growth as the magnetic field approaches saturation, and the fully saturated phase of the magnetic field. In order to capture these phases completely, the calculations are evolved for 100 crossing times, in contrast to only 10 in PF10. This is also intended to allow for high-quality time-averaged statistics to be obtained so that a meaningful comparison can be made.

The paper is structured as follows. Section 2 describes the details of the comparison. Results of the calculations are analysed in Section 3 and summarized in Section 4.

2 COMPARISON DETAILS

We compare the codes PHANTOM (SPMHD) and FLASH (grid). Both solve the ideal MHD equations but with fundamentally different numerical approaches: FLASH discretizes all fluid variables into fixed grid points, whereas PHANTOM discretizes the mass of the fluid into a set of Lagrangian particles that move with the fluid velocity. The calculations are performed for a series of resolutions, using 128^3 , 256^3 , and 512^3 resolution elements (grid points and particles, respectively).

2.1 Magnetohydrodynamics

We solve the ideal MHD equations, namely

$$\frac{d\rho}{dt} = -\rho \nabla \cdot \mathbf{v}, \quad (1)$$

$$\frac{d\mathbf{v}}{dt} = -\frac{1}{\rho}\nabla\left(P + \frac{B^2}{2\mu_0}\right) + \frac{1}{\mu_0\rho}\nabla\cdot(\mathbf{B}\mathbf{B}), \quad (2)$$

$$\frac{d\mathbf{B}}{dt} = (\mathbf{B}\cdot\nabla)\mathbf{v} - \mathbf{B}(\nabla\cdot\mathbf{v}), \quad (3)$$

where $d/dt = \partial/\partial t + \mathbf{v}\cdot\nabla$ is the material derivative, ρ is the density, \mathbf{v} is the velocity, P is the pressure, \mathbf{B} is the magnetic field, and μ_0 is the permeability of free space. The continuum equations have zero viscous and resistive dissipation (hence ideal). Since the growth rate of magnetic energy by small-scale dynamo amplification is set by dissipation, the growth rate in these calculations is set by the numerical dissipation present in the schemes. In Eulerian grid-based methods, numerical dissipation is introduced by the discretization of the advection term in the material derivative. By contrast, Lagrangian particle-based methods compute the material derivative exactly. The shock-capturing scheme is the other primary source of numerical dissipation. Modern grid-based methods use Riemann solvers, introducing numerical dissipation related to the accuracy of the shock reconstruction. The approach in particle methods is to explicitly add artificial viscous and resistive terms in order to capture shocks, using switches to tune the dissipation to the relevant discontinuity.

2.2 Initial conditions

The initial state is chosen to be simple so that both codes start from conditions which are identical. The initial density field is uniform with $\rho_0 = 1$, the velocity field is zero throughout ($\mathbf{v} = 0$), and the calculation is performed in a periodic box of length $L = 1$. An isothermal equation of state, $P = c_s^2\rho$, is used to calculate the pressure with sound speed $c_s = 1$. The magnetic field is set to $\sqrt{2} \times 10^{-5}$ in the z -direction. With $\mu_0 = 1$, this yields an initial plasma β , the ratio of thermal to magnetic pressure, of $\beta = P/P_{\text{mag}} = 10^{10}$. This initial magnetic field is certainly not representative of actual magnetic fields in molecular clouds, but is intentionally chosen to be weak to observe the exponential growth of magnetic energy via the small-scale dynamo.

2.3 Turbulent driving routine

As in PF10, supersonic turbulence was initiated and sustained at a root mean square (rms) Mach number of $\mathcal{M} = 10$ by an imposed driving force generated from an Ornstein–Uhlenbeck process (Eswaran & Pope 1988; Schmidt et al. 2009; Federrath et al. 2010). This is a stochastic process with a finite autocorrelation time-scale. The driving force can be decomposed in Fourier space into longitudinal and solenoidal modes. We assume purely solenoidal driving, so that the turbulence is driven primarily by vorticity rather than compression (cf. Federrath et al. 2011; Federrath 2013). However, one-third of the kinetic energy will still be contained in compressive modes due to the high Mach number of the turbulence (Federrath et al. 2010; Pan & Scannapieco 2010).

Consistency of the driving pattern between codes was achieved by pre-generating the time sequence of the Ornstein–Uhlenbeck modes, with both codes reading the pattern from file. The acceleration from the driving pattern is reconstructed at each individual cell or particle location by direct summation over all Fourier modes. The driving is at large scales, with a parabolic weighting of modes between $k_{\text{min}} = 1$ and $k_{\text{max}} = 3$, with smaller structures forming through turbulent cascade. The autocorrelation time-scale is $1t_c$,

Table 1. Input parameters for the turbulence driving routine.

| Parameter | Value |
|----------------------|--------------|
| Spectral form | 1 (parabola) |
| Solenoidal weight | 1 |
| Stirring energy | 8.0 |
| Autocorrelation time | 0.05 |
| Minimum wavenumber | 6.28 |
| Maximum wavenumber | 18.90 |
| Original random seed | 1 |

with t_c as defined in equation (4). The driving routine was developed by Federrath et al. (2010), and both the driving routine and the pattern file used in the paper are publicly available¹ with the input parameters used to generate the pattern file specified in Table 1. The stirring energy is used to obtain the variance of the Ornstein–Uhlenbeck process, corresponding to the autocorrelation time and energy input rate.

The relevant physical time-scale is the turbulent crossing time, which we define according to

$$t_c \equiv \frac{L}{2\mathcal{M}c_s}, \quad (4)$$

corresponding to $t_c = 0.05$ in code units. The turbulence was simulated for 100 crossing times, covering the full growth phase of the dynamo up until the magnetic energy reaches its saturation level, with at least half of the total time spent in the saturation phase.

2.4 PHANTOM – SPMHD

PHANTOM is a SPMHD code. The MHD equations (equations 1–3) are implemented as described in Price & Monaghan (2004a,b, 2005) and Price (2012), using Børve, Omang & Trulsen (2001)’s method of subtracting $\mathbf{B}(\nabla\cdot\mathbf{B})$ from the momentum equation to keep the magnetic tensile force stable. This implementation of momentum and induction equations resolves issues related to non-zero $\nabla\cdot\mathbf{B}$ in a manner that is equivalent to the Powell eight-wave approach (Powell 1994; Powell et al. 1999). In addition to this, we employ the constrained hyperbolic divergence cleaning method of Tricco & Price (2012), which is an SPMHD adaptation and improvement of the cleaning algorithm by Dedner et al. (2002). The cleaning wave speed is set to the local fast MHD wave speed. During the course of this work, it was found that if the wave speed included the term involving the relative velocity of particles (as in the artificial viscosity), then the individual time stepping scheme could introduce significant errors to the magnetic field. This occurred when particles were interacting on time step bins that were spaced too far apart. Using a time step limiter (i.e. Saitoh & Makino 2009) can prevent these errors, but for these calculations we simply reduce the cleaning speed by excluding the relative velocity.

Shocks are captured by adding an artificial viscosity, as described by Price & Monaghan (2004a, 2005) and based on the Monaghan (1997) formulation. It is important that the signal velocity, defining the characteristic speed of information propagation, includes a term involving the relative motion of particles to prevent particle interpenetration (Monaghan 1989), and as found by PF10, it is necessary

¹ The turbulent driving routine is bundled as part of the FLASH code (<http://flash.uchicago.edu/site/flashcode/>), and the pattern file used for these simulations is available at <http://cita.utoronto.ca/~tricco/mhdturbulence/>

to increase this by setting the dimensionless constant to $\beta_{AV} = 4$ for Mach 10 shocks (as opposed to the common $\beta_{AV} = 2$). We use the Morris & Monaghan (1997) switch to reduce dissipation away from shocks.

Discontinuities in the magnetic field are treated with an artificial resistivity (Price & Monaghan 2004a, 2005). PHANTOM uses a new switch we have recently developed to reduce dissipation of the magnetic field away from discontinuities (Tricco & Price 2013). This switch solves problems with the switch proposed by Price & Monaghan (2005), namely that it is able to capture shocks when the sound speed is significantly higher than the Alfvén speed (i.e. in the super-Alfvénic regime when the magnetic field is very weak). This is done by using the dimensionless quantity $h|\nabla\mathbf{B}|/|\mathbf{B}|$, which measures the relative strength of the discontinuity in the magnetic field.

The smoothing length (resolution length), h , of each particle is calculated in the usual manner by iteration of the density summation with $h = 1.2(m/\rho)^{1/3}$ using a Newton–Raphson solver (Price & Monaghan 2004b, 2007). This means that the numerical resolution scales with the density. For these set of simulations, the resolution increases by 4–8 \times in the highest density regions, with a decrease in resolution of about 2 \times in the lowest density regions. Time steps are set individual to each particle in a scheme that is block hierarchical in powers of two, with each particle setting its time step based on its local Courant condition. Second-order leapfrog time integration is used.

2.5 FLASH – grid code

FLASH² is a grid-based code using a finite volume scheme for solving the MHD equations (Fryxell et al. 2000; Dubey et al. 2008). Although FLASH can be used with adaptive mesh refinement (AMR; Berger & Colella 1989), our simulations employ a fixed and uniform Cartesian grid for simplicity. We here use FLASH with the HLL3R approximate Riemann solver for ideal MHD, based on a MUSCL–Hancock scheme (Waagan, Federrath & Klingenberg 2011). This is a predictor–corrector scheme and is second-order accurate in both space and time. Waagan et al. (2011) further show that this MHD scheme maintains $\nabla \cdot \mathbf{B} \sim 0$ to within negligible errors, by using divergence cleaning in the form of the parabolic cleaning method of Marder (1987) (see also Dedner et al. 2002). The MHD solver is particularly efficient and robust because it uses a relaxation technique that guarantees positive density and gas pressure and thus avoids unphysical states, by construction.

2.6 Computational cost

The FLASH calculations used 90, 1600, and 40 000 cpu-hours for the 128³, 256³, and 512³ simulations. The PHANTOM calculations used 2700 and 44 000 cpu-hours for the 128³ and 256³ simulations, and 280 000 cpu-hours for the 512³ calculation from $t = 0 \rightarrow 40t_c$. It is expected that each factor of 2 increase in resolution should increase the computational expense by 16 \times , since there are 8 \times more resolution elements and the Courant condition should reduce the time step by half. Both codes exhibit a scaling behaviour that is close to this. For PHANTOM, the particles are spread over $\sim 6, 7$, and 8 individual time step bins for the 128³, 256³, and 512³ resolution calculations, respectively. Approximately 35 per cent of the computational expense in the PHANTOM calculations is spent on neighbour

finding. The driving routine adds negligible computational expense (~ 2 per cent of overall cpu-hours).

FLASH uses distributed memory parallelization via message passing interface (MPI), with the 128³, 256³, and 512³ resolution calculations performed on 8, 64, and 512 cores, respectively. At the time these calculations were performed, the MPI implementation in PHANTOM was not finalized, so the PHANTOM calculations used shared memory parallelization via OpenMP, using 40 cores on a single node for all calculations. The FLASH calculations required 11, 25, and 80 wall clock hours, respectively, representing modest increases with resolution even though the cpu-hour cost increased by 20–25 \times for each factor 2 increase in resolution. The 128³ resolution PHANTOM calculation required 68 wall clock hours to be run to completion, but 1060 wall clock hours (~ 6 weeks) for the 256³ calculation. The difference in wall clock times between the two codes results from the differing parallelization methods, since PHANTOM, unlike FLASH, could not use additional cores for the higher resolution calculations in order to reduce the wall clock time. Overall, we find that, at comparable resolution, the PHANTOM calculations take roughly 30 \times more cpu-hours than the FLASH calculations, and that, as in PF10, the 256³ PHANTOM calculation takes approximately an equivalent amount of computational time as the 512³ FLASH calculation.

2.7 Analysis methods

2.7.1 Power spectra

Power spectra are calculated using the same analysis tool for both codes to ensure that results are comparable. The FLASH data are directly analysed with this tool, while the power spectrum of PHANTOM data is obtained by interpolating the particles to a grid of double the particle resolution (i.e. 256³ particles are interpolated to 512³ grid points). A higher resolution grid is chosen in order to represent the energy contained in the highest density structures, which are up to 4–8 \times higher than the initial resolution. Appendix A investigates the effect of the resolution of the interpolated grid, in addition to the difference between mass and volume weighted interpolation. We found that the magnetic field was satisfactorily represented by a grid which has twice the resolution of the particle calculation.

2.7.2 Probability distribution functions

Computing a volume-weighted PDF from grid methods involves binning the cells according to the value of the quantity and normalizing such that the integral under the PDF is unity. For SPH this is more complicated since the resolution is tied to the mass rather than the volume. PF10 computed the PDF directly from the SPH particles by weighting the contribution of each particle, i , by the volume element m_i/ρ_i . Price, Federrath & Brunt (2011) later found that this was inaccurate at high Mach number because $\sum_i m_i/\rho_i$ has no requirement that it equals the total volume. Instead, one should interpolate to a fixed volume using the SPH kernel W , since m_i/ρ_i is only meaningful when multiplied by the kernel (since SPH is derived assuming $\sum_i m_i/\rho_i W(\mathbf{r} - \mathbf{r}_i, h) = 1$). However, interpolation to a fixed grid (e.g. Kitsionas et al. 2009) is also problematic since the resolution in our simulations is 4–8 \times higher in the densest regions compared to a fixed grid with the same number of resolution elements. Hence, sampling the high-density tail of the SPH calculation would require a commensurably high-resolution grid. We follow Price et al. (2011) in using an adaptive mesh to compute the PDF from the SPH particles, where the mesh is refined until the

² <http://flash.uchicago.edu/site/flashcode>

cell size is smaller than the smoothing length. The SPH PDF is then computed and normalized directly from this adaptive mesh.

3 RESULTS

We focus of the analysis of our calculations on effects produced by the small-scale dynamo. Since this comparison uses the same codes, initial conditions, and turbulent driving routine as the hydrodynamic turbulence comparison of PF10, analyses performed by PF10 have only been repeated where the addition of magnetic fields would be expected to alter the result (i.e. for the density PDF).

We analyse the three phases of small-scale dynamo amplification throughout this section: (i) the steady, exponential growth of magnetic energy; (ii) the slow linear or quadratic growth of magnetic energy once the magnetic field is saturated on the smallest scales; and (iii) the fully saturated phase of magnetic energy. Since we assume ideal MHD, the numerical dissipation varies with resolution thus the kinetic and magnetic Reynolds numbers are not constant. This affects the growth rate and saturation level of magnetic energy, which enable us to contrast the scaling behaviour of the two methods.

3.1 Formation of the turbulence; $t/t_c \lesssim 2$

The simulations begin with a brief transitory phase while the turbulence is formed by the driving routine. Fig. 1 shows slices of ρ and $|B|$ at $z = 0.5$ for $t/t_c = 1$, shortly after large shocks have been formed by the driving routine and started to interact. The magnetic field is strongest in regions where the density is highest due to compression of the magnetic field in the shocks. Conversely, the low-density regions exhibit relatively weaker magnetic fields.

Approximately half a crossing time is required for the kinetic energy to saturate (see Fig. 2), since the large-scale shocks contain the bulk of the kinetic energy, though it takes another turbulent crossing time before the turbulence is fully developed at smaller spatial scales. The magnetic energy is amplified by two orders of magnitude during the transient phase while the turbulence is developing (Fig. 2). This occurs in two steps. First, for $t/t_c \lesssim 1$, a sharp rise in magnetic energy is caused by the formation of large-scale shocks (Fig. 1). Second, from $t/t_c \approx 1-2$, the magnetic energy increases exponentially during the generation of small-scale structure in the density and magnetic fields caused by the interaction of the shocks, but at a rate higher by a factor of 2–3 than the measured rate in the exponential growth phase (Section 3.3). Once the turbulence is fully developed on all spatial scales, the magnetic field enters the steady, exponential growth phase of the small-scale dynamo.

The initial transient growth of the magnetic field is resolution dependent, with higher resolutions resulting in higher magnetic energy by the time the turbulence is fully developed. For example, the magnetic energy in the 512^3 PHANTOM calculation is increased by an additional 3–4 orders of magnitude compared to the other calculations. We have investigated whether this growth is merely a numerical artefact of the time stepping by re-doing the initial phase with a reduction in the Courant factor, and also by using global time steps instead of individual time steps. These did not alter our results. Additionally, we checked if this growth is driven by spurious generation of divergence of the magnetic field by both turning off the hyperbolic divergence cleaning (no divergence control), and conversely by increasing the hyperbolic cleaning wave speed by a factor of 10 (matching the rms velocity; see the overcleaning method in Tricco 2015). These showed the same fast transient magnetic field growth, so this is not caused by unphysical magnetic field growth

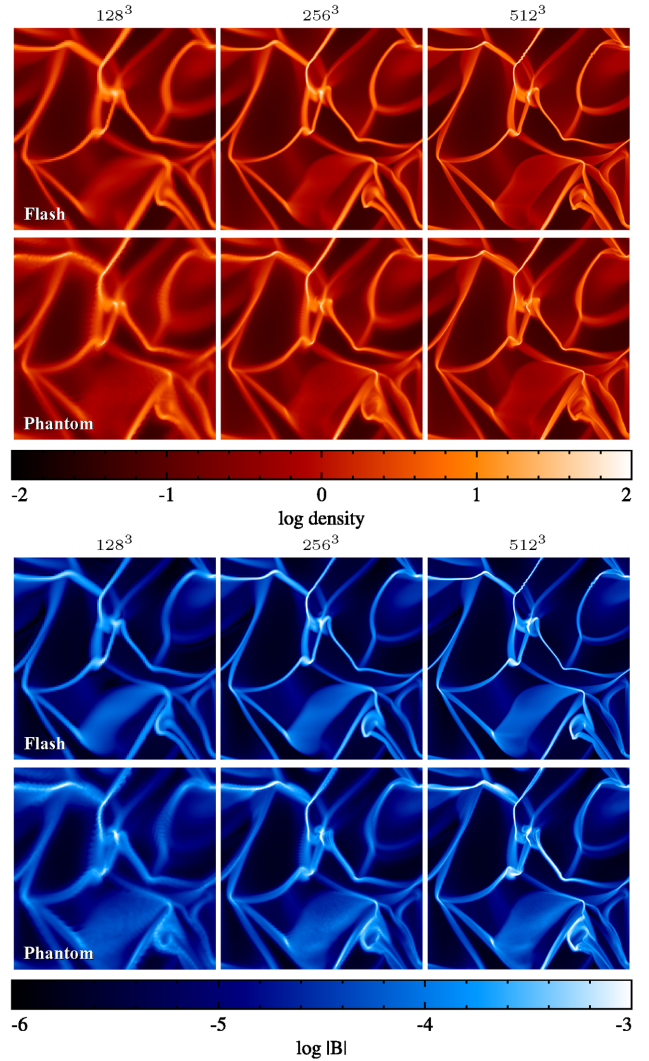


Figure 1. Slices of ρ (top) and $|B|$ (bottom) in the $z = 0.5$ mid-plane at $t/t_c = 1$ during the initial formation of the turbulence. The results from FLASH (top row) and PHANTOM (bottom row) are shown for resolutions of 128^3 , 256^3 , and 512^3 (left to right). As the resolution is increased, the shock lines become more well defined. The regions with highest magnetic field strength are in the dense shocks.

in the form of high $\nabla \cdot \mathbf{B}$. Hence, the growth of magnetic energy in the PHANTOM simulations appears to be physical, originating from the explicitly added dissipation terms rather than occurring due to numerical error or instability.

3.2 Column integrated density and magnetic field strength

Fig. 3 shows a time sequence of column density and column integrated $|B|$ from $t/t_c = 2-8$, comparing FLASH (top figure) and PHANTOM (bottom figure) calculations at 256^3 since the growth rates are similar at this resolution (cf. Fig. 2 and Table 2). Both codes show similar patterns in column density and magnetic field for the first few crossing times (left two columns), but eventually the patterns diverge due to the chaotic, non-deterministic nature of turbulence (right two columns) This was also found in PF10.

There exists a definite correlation between the high-density regions with the regions of strongest magnetic field when compared at a fixed time for each code individually. This is caused in part

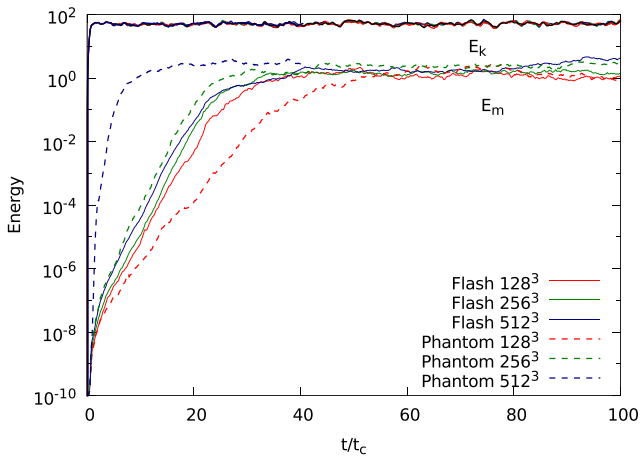


Figure 2. Growth and saturation of the magnetic energy for FLASH and PHANTOM at resolutions of 128^3 , 256^3 , and 512^3 grid points and particles. The steady, exponential growth of magnetic energy by the small-scale dynamo can be clearly seen in all calculations, along with the slow turnover of magnetic energy growth as the dynamo begins to saturate the magnetic energy and it enters the linear or quadratic growth phase. Both codes saturate the magnetic energy at similar levels. FLASH has similar magnetic energy growth rates across the resolutions simulated, while PHANTOM exhibits faster growth rates with increasing resolution. This resolution dependence is a consequence of the artificial dissipation terms used for shock capturing. The top lines are the kinetic energy for the six calculations, kept at a steady level by the turbulent driving routine.

due to the compression of the gas, as similarly evidenced during the initial formation of the turbulence (Section 3.1). Despite the high-density regions having the highest magnetic field strength, the mean magnetic field strength throughout the domain can be seen to be increasing with time, a signature of the small-scale dynamo. This is quantitatively examined in Section 3.6 by computing the power spectrum of the magnetic energy.

3.3 Exponential growth rate of magnetic energy

The evolution of the magnetic energy as a function of time is shown in Fig. 2 for the calculations from both PHANTOM and FLASH using 128^3 , 256^3 , and 512^3 resolution elements (see legend). To compare the exponential growth rate of magnetic energy between the calculations, the magnetic energy in Fig. 2 during the exponential growth phase, defined between $t/t_c = 3$ and the onset of the slow growth phase, was fitted to $E_m \propto \exp(\Gamma t/t_c)$, where Γ is the growth rate. The growth rates are given in Table 2. The FLASH results all have similar growth rates. In contrast, the PHANTOM results have growth rates that increase with resolution by nearly a factor of 2 for each doubling of resolution.

Analytic studies of the exponential growth rate of the small-scale dynamo have shown that for $\text{Pm} \ll 1$, the growth rate scales with $\text{Rm}^{1/2}$, while for $\text{Pm} \gg 1$, it scales with $\text{Re}^{1/2}$ (Schober et al. 2012a; Bovino et al. 2013). Theoretical predictions of the growth rate for $\text{Pm} \sim 1$, which is the Prandtl number regime for numerical codes in the absence of explicit dissipation terms, are more uncertain. The growth rate in the transition region between $0.1 < \text{Pm} < 10$ was probed by Federrath et al. (2014) using FLASH simulations with explicit viscous and resistive dissipation. They found that the magnetic energy growth rate for $\text{Pm} \lesssim 1$ exhibited a steep dependence on Pm and only agreed qualitatively with the analytical expectations of Schober et al. (2012a) and Bovino et al. (2013). Conversely, the

growth rate for $\text{Pm} \gtrsim 1$ quantitatively agreed with analytical expectations, with, by comparison, relatively little variation with respect to Pm .

Federrath et al. (2011) measured the effective Prandtl number in FLASH through comparison with calculations with physical dissipation terms, finding that $\text{Pm} \sim 2$. This is in agreement with similar experiments by Lesaffre & Balbus (2007). For PHANTOM, the effective Prandtl number can be estimated analytically from the artificial dissipation terms, for which we find that $\text{Pm} \sim 1$ for these calculations (see Appendix B for further discussion). Though the theory for the growth rate around $\text{Pm} \sim 1$ is still uncertain, our results appear to be in agreement with those of Federrath et al. (2014).

To further understand the dependence of the growth rate on resolution for PHANTOM, a series of calculations were performed where the dimensionless parameters α and α_B in the artificial viscosity and resistivity terms were fixed to different values. We found that the growth rate depended on the amount of artificial dissipation applied, and produced an effect equivalent to changing the resolution (Fig. 4). Since the dissipation in PHANTOM is proportional to resolution, we conclude that the growth rates obtained in our comparison are consistent with the expected resolution scaling of the artificial dissipation terms. We comment that using $\alpha_B = 8$ for a resolution of 128^3 particles would produce a magnetic Reynolds number of $\text{Rm} \sim 160$ (cf. Appendix B), below estimates of the critical magnetic Reynolds number needed to support dynamo amplification (Schober et al. 2012a).

3.4 Magnetic energy saturation level

The mean magnetic energy of the saturated magnetic field is approximately 2–4 per cent of the mean kinetic energy for all calculations (Table 2). This is consistent with theoretical predictions (Schober et al. 2015) and prior numerical studies (Federrath et al. 2011, 2014) of the small-scale dynamo in compressible, high Mach number turbulence. We note that incompressible turbulence has a higher saturation value, approaching 10–40 per cent of the kinetic energy (Brandenburg et al. 1996; Haugen, Brandenburg & Dobler 2004; Cho et al. 2009).

The mean magnetic energy exhibits a trend of increasing with resolution, with the 512^3 calculations twice as high as the corresponding calculations at 128^3 (for both FLASH and PHANTOM), though remains within the standard deviation. We note that the 512^3 PHANTOM calculation is averaged over a shorter time ($20t_c$ compared to $50\text{--}70t_c$), which is reflected by its smaller standard deviation. The 512^3 FLASH calculation shows a long-term variation, with a 50 per cent increase in mean energy above $80t_c$. This is reflected in the wider standard deviation in this calculation (~ 1.0 compared to $0.2\text{--}0.3$ in the 128^3 and 256^3 calculations). Overall, while the statistical ranges of mean energy overlap between resolutions, it appears that PHANTOM yields higher mean magnetic energy during the saturation phase than FLASH at comparable resolution.

A set of PHANTOM calculations were performed keeping the same artificial viscosity parameters but turning off the Tricco & Price (2013) switch for artificial resistivity (i.e. using a constant artificial resistivity parameter, $\alpha_B = 1$), thereby increasing the amount of resistive dissipation and lowering the magnetic Reynolds number. This reduced the mean magnetic energy in the saturation phase at all three resolutions (128^3 : 1.52 reduced to 1.01; 256^3 : 2.31 to 1.32; 512^3 : 2.98 to 1.57). Considering that the Prandtl number in FLASH should be nearly constant with varying resolution (Appendix B), this suggests that the magnetic Reynolds number determines the saturation level of the magnetic field.

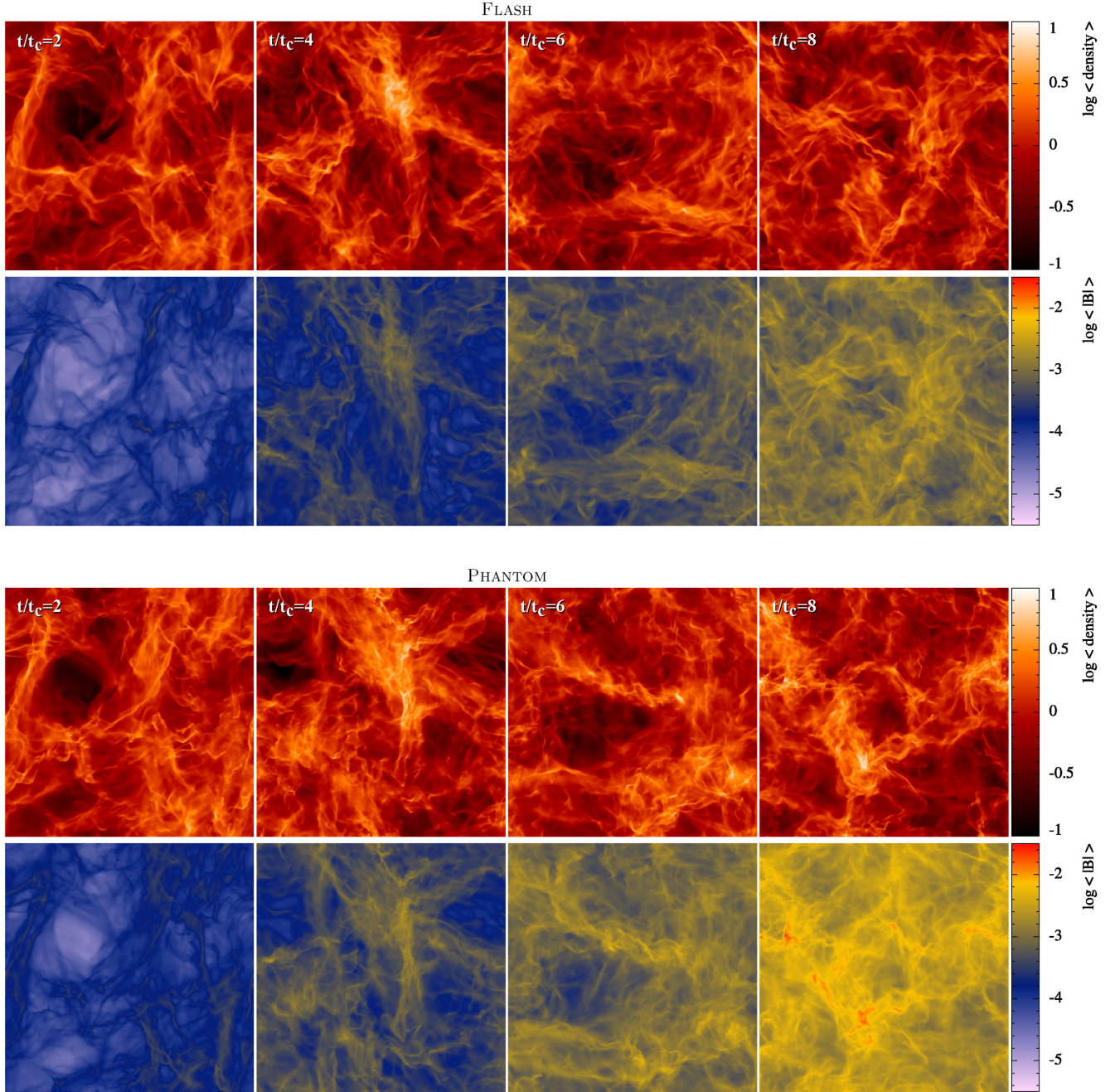


Figure 3. z -column integrated ρ and $|B|$, defined $\langle B \rangle = \int |B| dz / \int dz$, for FLASH (top) and PHANTOM (bottom) at resolutions of 256^3 for $t/t_c = 2, 4, 6, 8$. The density field has similar structure in both codes at early times, but diverge at late times due to the non-deterministic behaviour of the turbulence. The magnetic field is strongest in the densest regions, while the mean magnetic field strength throughout the domain increases with time.

Table 2. The growth rate (Γ) of magnetic energy during the exponential growth phase, defined $\propto \exp(\Gamma t/t_c)$, and the time-averaged saturation values of kinetic and magnetic energy.

| Calculation | Γ | $\langle E_k \rangle_{\text{sat}}$ | $\langle E_m \rangle_{\text{sat}}$ |
|-----------------|----------|------------------------------------|------------------------------------|
| FLASH 128^3 | 0.69 | 51.11 ± 5.51 | 1.20 ± 0.31 |
| FLASH 256^3 | 0.75 | 51.19 ± 4.81 | 1.46 ± 0.20 |
| FLASH 512^3 | 0.74 | 52.17 ± 5.15 | 2.36 ± 1.02 |
| PHANTOM 128^3 | 0.47 | 50.30 ± 4.80 | 1.52 ± 0.48 |
| PHANTOM 256^3 | 0.78 | 51.17 ± 5.34 | 2.31 ± 0.47 |
| PHANTOM 512^3 | 1.63 | 51.79 ± 3.94 | 2.98 ± 0.35 |

3.5 Alfvénic Mach number

Fig. 5 shows the time evolution of the rms Alfvén speed, v_A , and rms Alfvénic Mach number, \mathcal{M}_A , for all six calculations. The initial rms Alfvénic Mach number is $\mathcal{M}_A \sim 10^6$, which decreases as the dynamo amplifies the magnetic energy and the rms Alfvén speed throughout the domain increases. In the saturation phase, the rms Alfvén speed is approximately twice the sound speed ($v_A \sim 2c_s$) and the rms Alfvénic Mach number is $\mathcal{M}_A \sim 20$. In other words, the turbulence remains super-Alfvénic even once the magnetic field has reached saturation. The Alfvénic Mach number in Fig. 5 is calculated by taking the rms of the local \mathcal{M}_A as calculated per

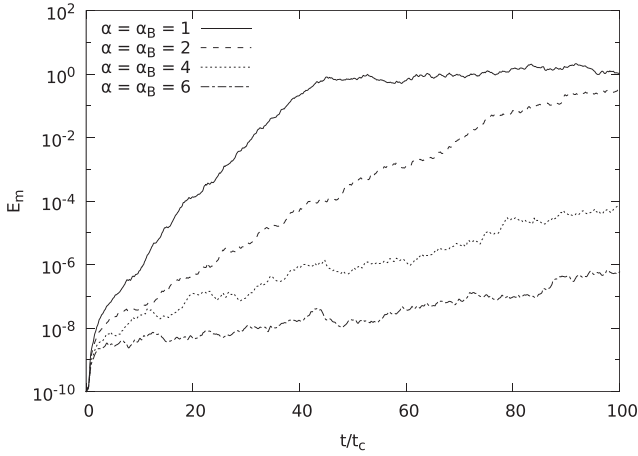


Figure 4. A 128^3 PHANTOM calculation where the artificial viscosity and resistivity parameters are systematically increased (no switches are used). With increasing dissipation, the growth rate decreases, producing the same behaviour consistent with changes in resolution.

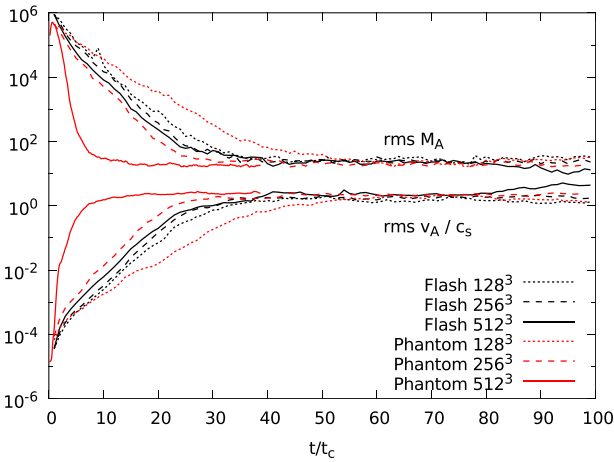


Figure 5. Time evolution of the rms Alfvén speed and Alfvénic Mach number. For all calculations, the time averaged rms Alfvén speed in the saturation phase is $v_A \sim 2c_s$. The rms Alfvénic Mach number is $M_A \sim 20$, as calculated per cell or particle. This noticeably differs from the rms velocity divided by the rms Alfvén speed (~ 5).

grid cell or particle. This differs by a factor of 4 to that calculated by dividing the rms velocity (10) by the rms v_A (2), yielding ~ 5 , suggesting a correlation between the velocity and magnetic field.

3.6 Magnetic energy power spectra

That the total magnetic field is growing in strength – and not just in isolated regions – may be quantified by examining the power spectra of the magnetic energy, $P(B)$. The magnetic energy spectra during the growth phase for the six calculations are presented in Fig. 6. The magnetic energy can be seen to grow uniformly at all spatial scales in all six calculations (indicated by the translation of the power spectrum along the y-axis in the plots with minimal change in the shape), behaviour consistent with the small-scale dynamo (Maron, Cowley & McWilliams 2004; Schekochihin et al. 2004c; Brandenburg & Subramanian 2005; Cho et al. 2009; Bhat & Subramanian 2013; Federrath et al. 2014).

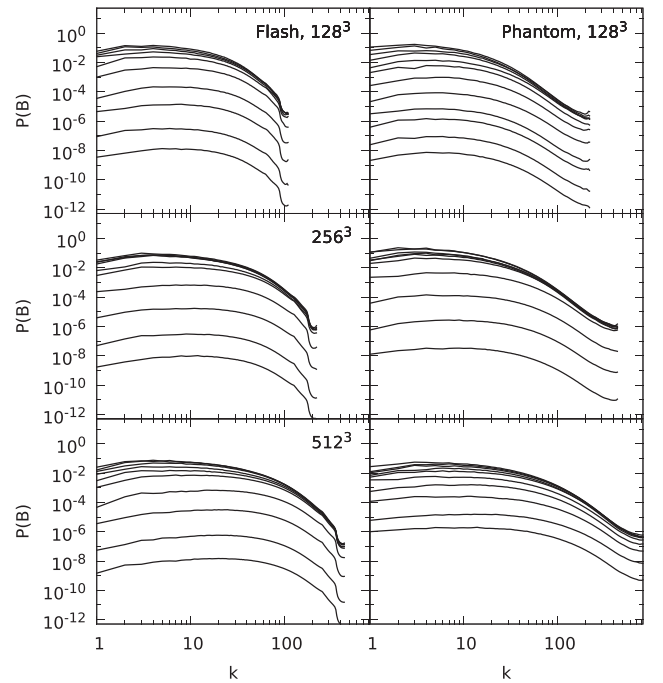


Figure 6. Spectra of the magnetic energy during the growth phase for FLASH (left) and PHANTOM (right) for resolutions of 128^3 , 256^3 , and 512^3 (top to bottom). Each spectral line is sampled at intervals of $5t/t_c$ up to $t/t_c = 50$, except for the 512^3 PHANTOM run which is sampled every t/t_c (from $t/t_c = 2-12$). The magnetic field grows equally at all spatial scales for all calculations. The saturation of the magnetic energy occurs first at the smallest scales, with a time delay before the larger scales saturate.

All of the spectra have the same general shape, with a decrease in spectral energy at and above the driving scale ($k \leq 3$) and a more-or-less flat spectrum ($P(B) \approx \text{constant}$) between $3 < k < 10$ for the 128^3 calculations, extending to $k \sim 20$ and ~ 40 for the 256^3 and 512^3 calculations. The dissipation range in the PHANTOM results extends further to smaller scales than the FLASH results for a particular resolution. The maximum in the magnetic energy spectrum in both codes occurs at high wavenumbers, as expected for small-scale dynamos (Cho & Vishniac 2000; Brandenburg, Sokoloff & Subramanian 2012), occurring around the high k end of the ‘relatively’ flat region of the spectra.

Fig. 6 shows that the magnetic energy saturates first at small scales. This is characteristic of the small-scale dynamo since this is where magnetic energy is being injected (Cho et al. 2009). It is expected that the magnetic energy will grow linearly at this stage, though for Burgers turbulence, which is closer to the regime our simulations are in, it is expected that the magnetic energy growth will be closer to quadratic (Schleicher et al. 2013). This slow growth phase lasts until the reverse cascade of magnetic energy saturates all spatial scales. This turnover in magnetic energy growth may be clearly seen in the 128^3 and 512^3 PHANTOM growth curves in Fig. 2.

Fig. 7 shows a cross-section of the power spectrum evolution at $k = 5, 40$, and 100 for the 256^3 calculations. These scales were chosen to represent large, medium, and small-scale structure. This shows that the magnetic field grows in the same manner at all scales in both codes. It is also evident that the magnetic field enters the slow growth phase first at high wavenumbers.

Fig. 8 shows the time-averaged spectra of the magnetic energy from all six calculations in the saturation phase, with the shaded regions showing one standard deviation of the time average. In each

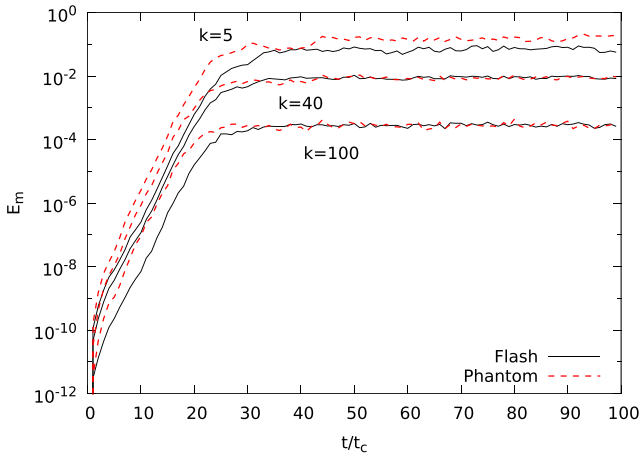


Figure 7. Spectra of the magnetic energy at the $k = 5, 40,$ and 100 bands as a function of time for the 256^3 resolution calculations of FLASH (black lines) and PHANTOM (red dashed lines). The growth rate at these different wavenumbers is nearly identical. The saturation level is the same between the two codes for $k = 40, 100$, with PHANTOM containing ~ 2 times as much energy in the large-scale $k = 5$ band.

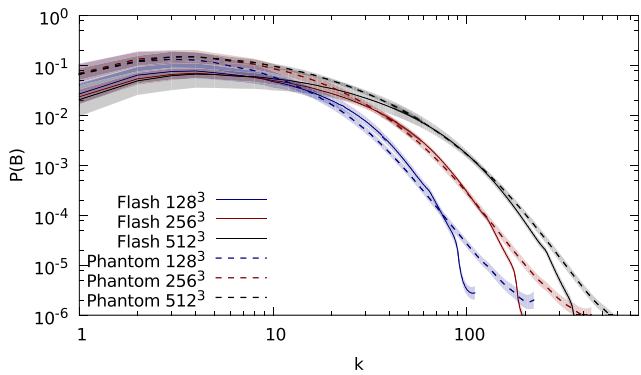


Figure 8. Time averaged spectra of the magnetic energy in the saturation phase for FLASH (solid lines) and PHANTOM (dashed lines) at resolutions of 128^3 (blue), 256^3 (red), and 512^3 (black). Shaded regions represent the standard deviation. The PHANTOM calculations systematically contain more magnetic energy (approximately $2\times$) in large-scale structure ($k < 10$) compared to FLASH, and have an extended tail at high k due to the adaptive resolution.

case 50 spectra have been averaged over a minimum of $50t_c$, with the exception of the 512^3 PHANTOM calculation which has been averaged over $20t_c$. The spectra of FLASH and PHANTOM are similar in shape, except that the PHANTOM calculations contain approximately twice as much magnetic energy in large-scale structure ($k < 10$). This is consistent with the higher mean magnetic energy in the PHANTOM calculations in Table 2, indicating that this energy is stored in the largest scales of the field.

The peak of the magnetic energy spectra for both codes is at $k \sim 3-4$, occurring just above the driving scale. As the resolution is increased, both codes extend the spectra further towards small scales. The FLASH power spectra drop sharply at the Nyquist frequency, while the PHANTOM power spectra reach higher wavenumbers than FLASH for the same number of resolution elements. While, in SPH, the smoothing kernel will distribute power to higher wavenumbers, the PHANTOM calculations have adaptive resolution that reach $4-8\times$ that of the FLASH calculation in the densest regions. For that reason, the PHANTOM power spectra have been analysed on a grid that is

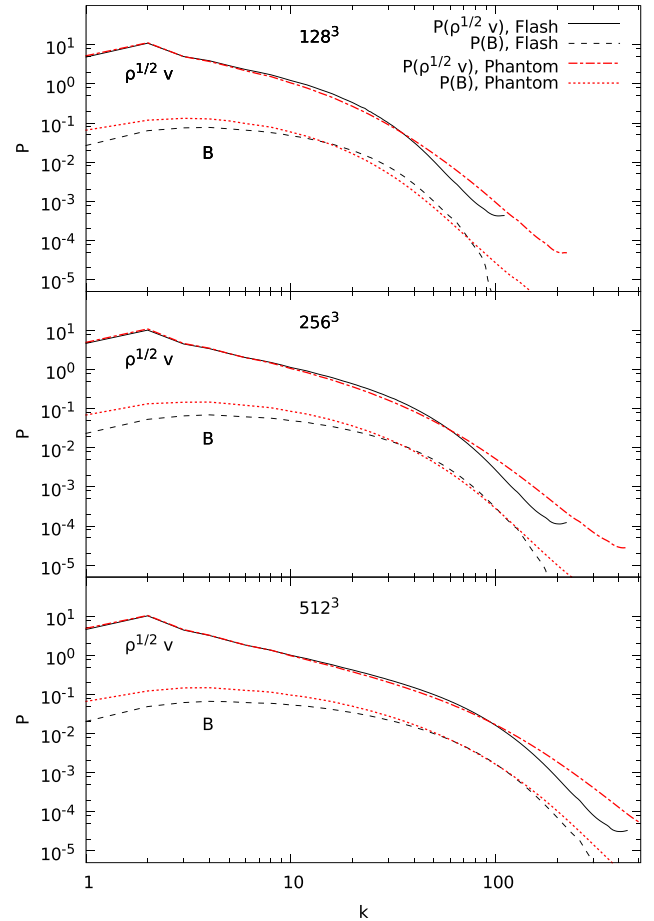


Figure 9. Time averaged kinetic ($\rho^{1/2}v$) and magnetic (B) energy spectra in the saturated phase for FLASH (black lines) and PHANTOM (red lines). As the resolution is increased, the kinetic and magnetic energy spectra extend to higher wavenumbers, with the magnetic energy lower than kinetic energy at all wavenumbers.

twice the resolution of the FLASH grid (see Appendix A for why this grid resolution was chosen), and it is expected that these power spectra correspond to resolved structures.

Fig. 9 compares the magnetic spectra to the kinetic energy spectra. It is characteristic for the small-scale dynamo for the peak in the magnetic energy spectrum to be at a wavenumber just above the peak in the kinetic energy spectrum (Cho & Vishniac 2000; Brandenburg et al. 2012). This is clearly seen in Fig. 9. The sharp peak at $k = 2$ in the kinetic energy spectra is due to the driving force, and for all resolutions the peak of the magnetic energy spectra occurs just above this scale ($k \sim 3-4$).

The magnetic energy is lower than the kinetic energy at all wavenumbers. Brandenburg et al. (1996), Schekochihin et al. (2004c), Maron et al. (2004), Haugen, Brandenburg & Dobler (2004), and Cho et al. (2009) found that the magnetic energy spectrum overtook the velocity spectrum, $P(v)$, at high k in incompressible and subsonic calculations. We similarly found that the magnetic energy spectra of our calculations exceeded the velocity spectra at high k (without taking into account the density field), but since we are dealing with compressible, supersonic turbulence, we instead investigate the kinetic energy spectrum, i.e. $P(\rho^{1/2}v)$. In this case, the magnetic energy spectrum is below the kinetic energy spectrum at all wavenumbers for both FLASH and PHANTOM.

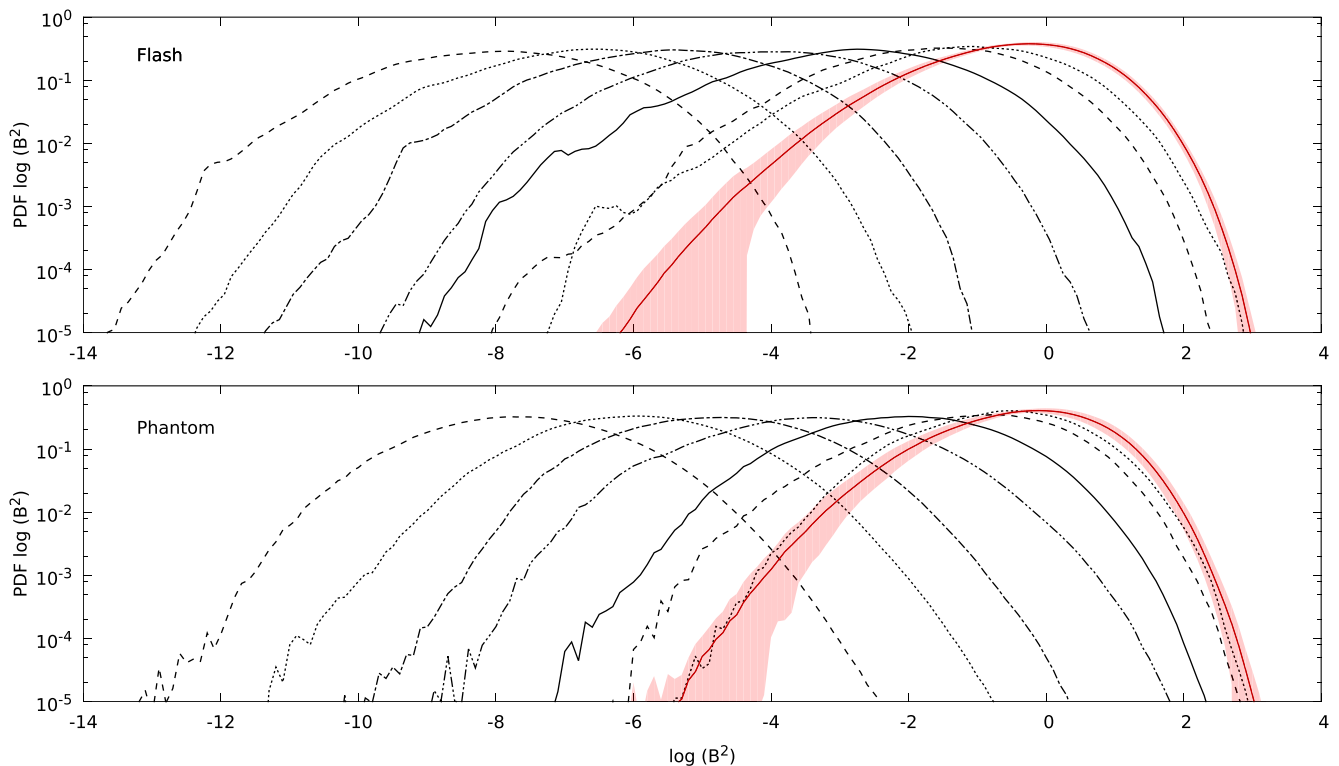


Figure 10. PDF of $\log(B^2)$ during the growth phase, with the red line time averaged during the saturation phase. The top panel shows the FLASH calculation, with the bottom panel the PHANTOM calculation. The PDF has a log-normal distribution during the growth phase, maintaining its width while the peak smoothly translates to higher magnetic field strengths. As the strongest magnetic fields saturate, the PDFs become lop-sided. Both PDFs in the saturation phase have similar peaks and high-end tails, with FLASH exhibiting a slightly extended low-end tail.

3.7 PDFs of B^2

Fig. 10 shows the time evolution of the PDF of B^2 for the 256^3 calculations. The instantaneous PDFs are shown from $t/t_c = 4$ – 28 at intervals of $\Delta t = 4t_c$, with the time-averaged PDF during the saturation phase given by the red line with the shaded region representing the standard deviation of the time-averaging. The shape of the PDFs remains mostly log-normal during the growth phase. As the dynamo amplifies the magnetic field, the PDFs maintain their width and shape, with the peak simply translating to higher magnetic field strengths. In other words, the distribution of magnetic fields does not broaden over time, but all magnetic field strengths are increased uniformly such that the PDFs maintain their shape and width while the mean increases (Schekochihin et al. 2004b,c).

The PDFs become distorted during the slow growth phase as the magnetic field approaches saturation. Once the dynamo enters the slow growth regime, it is no longer able to amplify the strongest magnetic fields due to the back-reaction of the Lorentz force. Thus, the high-end tail of the distribution anchors in place, leading to a ‘squeezed’ distribution as the magnetic fields in the peak and low-end tail continue to increase (Schekochihin et al. 2004b,c). This produces a lop-sided distribution and both codes show this behaviour as the magnetic field saturates. This may also be seen in Fig. 11 which shows the PDF of B^2 on a linear scale.

In the saturation phase, the distributions peak at similar magnetic field strengths, agreeing to within 10 per cent on the maximum of the peak. They have similar ranges on the high-end tail of the distribution, and the maximum magnetic field achievable agrees to within 10 per cent. The low-end tail extends further for FLASH, and has a larger standard deviation. From the linearly scaled plots of

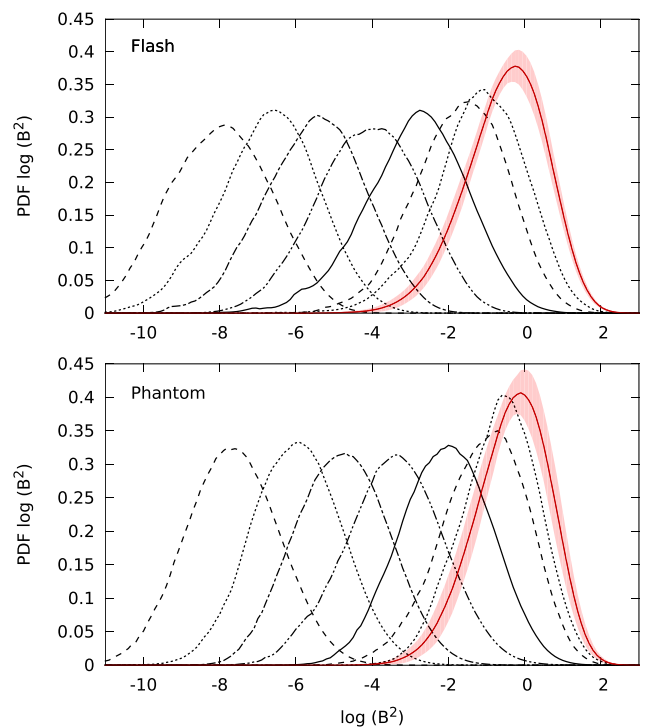


Figure 11. PDF of $\log(B^2)$ during the growth phase, with the red line time averaged during the saturation phase. This is equivalent to Fig. 10 but on a linearly scaled plot. In the saturation phase, the distribution is skewed with smaller deviation of magnetic field strengths.

Fig. 11, it is seen that the probability of being at the mean magnetic field strength increases by ~ 20 per cent once the magnetic field has saturated, corresponding to a reduced variance in the distribution of magnetic field strengths. This occurs due to the saturation of the strongest magnetic fields (Schekochihin et al. 2004b,c).

Fig. 10 additionally shows that FLASH is able to sample lower magnetic field strengths compared to PHANTOM, which was similarly noted by PF10 in the density PDFs and was attributed to the better weighting of resolution elements towards low-density regions in the grid code. The extended low-end tail of the PDFs of B^2 for the grid code is consistent with this, since the low-density regions are expected to contain weaker magnetic fields.

3.8 Density PDFs

For supersonic turbulence, the PDF of $s \equiv \ln(\rho/\rho_0)$ follows a log-normal distribution (e.g. Vazquez-Semadeni 1994; Padoan, Nordlund & Jones 1997; Passot & Vázquez-Semadeni 1998; Nordlund & Padoan 1999; Klessen 2000; Federrath, Klessen & Schmidt 2008; Lemaster & Stone 2008; Federrath et al. 2010; Price & Federrath 2010; Kritsuk, Norman & Wagner 2011a; Federrath & Klessen 2013). For the motivation behind this choice of variable, s , see Vazquez-Semadeni (1994) and Federrath et al. (2008). This log-normal distribution is a consequence of the density at a location being perturbed randomly and independently over time, which according to the central limit theorem, will converge to a log-normal distribution (Papoulis 1984; Vazquez-Semadeni 1994). Other processes may affect the shape of the PDF. Higher Mach numbers broaden the width of the distribution (Kowal, Lazarian & Beresnyak 2007; Lemaster & Stone 2008; Federrath et al. 2010; Price et al. 2011; Konstandin et al. 2012), self-gravity has been demonstrated to add power-law tails at high densities (Klessen 2000; Li, Klessen & Mac Low 2003; Kritsuk, Norman & Wagner 2011a; Federrath & Klessen 2013; Girichidis et al. 2014), non-isothermal equations of state can introduce power-law tails at high and low densities (Passot & Vázquez-Semadeni 1998; Li, Klessen & Mac Low 2003; Federrath & Banerjee 2015; Nolan, Federrath & Sutherland 2015), different forcing mechanisms (compressive versus solenoidal) influence the shape of the distribution (Federrath et al. 2008, 2010; Federrath 2013), and, relevant for the current discussion, magnetic fields can narrow the width of the distribution by effectively decreasing the compressibility of the gas (Padoan & Nordlund 2011; Collins et al. 2012; Molina et al. 2012; Federrath & Klessen 2013).

PF10 compared the PDF of s for hydrodynamic turbulence, finding that SPH yielded a log-normal distribution as expected. There were differences when compared to PDFs obtained with grid-based methods. In particular, the density PDF obtained with SPH extended further to higher densities, but conversely had a shorter low-end tail. This was a consequence of the resolution in SPH being adaptive in density, i.e. high-density regions have more resolution. Now we consider how the addition of magnetic fields may affect the density PDF in SPMHD.

Fig. 12 compares the PDFs of the density contrast, s , during the growth phase, while the magnetic field is dynamically weak, to the saturation phase when the magnetic field is at its strongest. The PDFs in the growth phase were time-averaged during the first half of the growth phase while $E_m < 10^{-4}$ (excluding the initial transient growth). This allows for statistical averaging over a number of crossing times while the magnetic field is still dynamically weak. The PDFs in the saturation phase were averaged over at least $50t_c$, except the 512^3 PHANTOM calculation averaged over $20t_c$. The standard deviation from the time averaging is shown for the highest

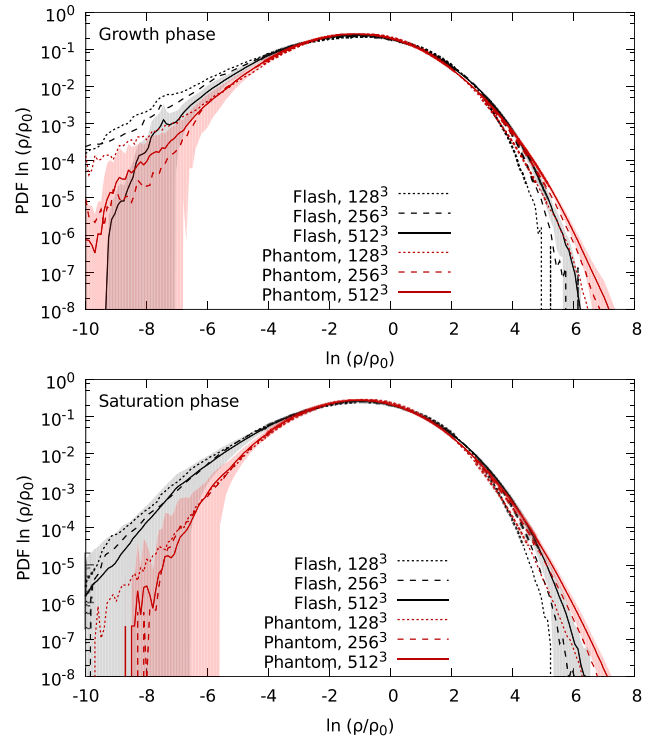


Figure 12. Time averaged density PDFs during the growth phase (top panel, for $t/t_c = 2-10$) and during the saturation phase (bottom panel, for $t/t_c = 30-100$, only $t \geq 50$ for the 128^3 PHANTOM calculation). The peaks and high-end tail of the PDF are similar for both cases, but the low-density tail is less extended when the magnetic field has reached saturation.

resolution calculations by the shaded regions (black for FLASH, red for PHANTOM).

Both codes show PDFs close to a log-normal distribution in both the growth and saturation phases. FLASH can be seen to sample a lower range of densities, while PHANTOM samples a higher range. This behaviour is similar to that found by PF10, and occurs because PHANTOM uses adaptive resolution based on the density. In the saturation phase, the extra support from magnetic pressure reduces the low-end tail of the distribution, making it more log-normally distributed, consistent with previous findings (Kowal et al. 2007; Lemaster & Stone 2008; Price et al. 2011; Molina et al. 2012; Federrath & Klessen 2013). The peak and high-end tail of the distribution remain quite similar during both the growth and saturation phases. Fig. 13 shows the PDFs of s on a linear scale. As before, the extended low-end tail for FLASH is visible, but from this it is also clear that the mean of the distribution is higher for PHANTOM, meaning that the distribution is slightly narrower. This was also noted by PF10.

4 CONCLUSION

We have performed a comparison of particle-based SPMHD methods using the PHANTOM code with results from the grid-based code FLASH on the small-scale dynamo amplification of magnetic fields. The calculations used supersonic turbulence driven at rms velocity Mach 10 in an isothermal fluid contained in a periodic box. The initial magnetic field was uniform and had an energy 12 orders of magnitude smaller than the mean kinetic energy of the turbulence. The small-scale dynamo amplification of the magnetic field was followed for 10 orders of magnitude in energy.

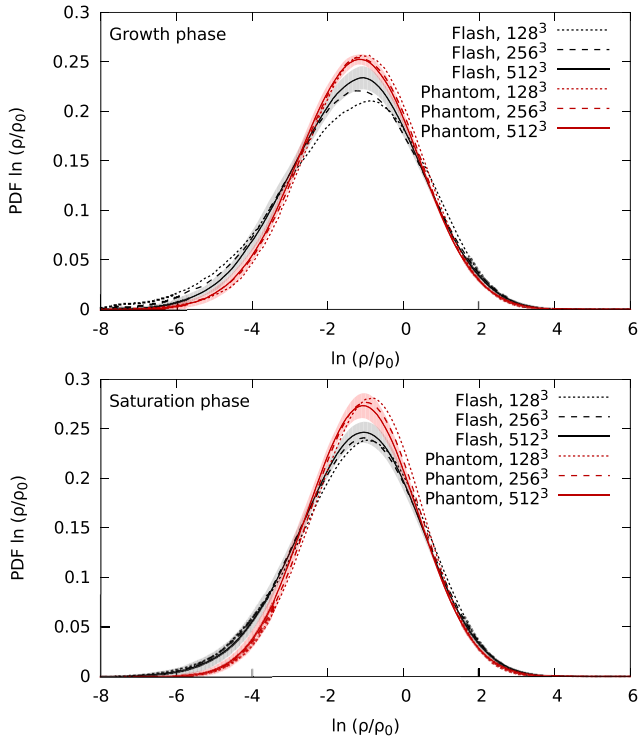


Figure 13. Time-averaged density PDFs during the growth phase (top panel, for $t/t_c = 2-20$) and during the saturation phase (bottom panel, for $t/t_c = 30-100$, only $t/t_c \geq 50$ for the 128^3 PHANTOM calculation). This is equivalent to Fig. 12 but on a linearly scaled plot. The peaks and high-end tail of the PDF are similar for both cases, but the low-density tail is less extended when the magnetic field has reached saturation.

The three phases of small-scale dynamo amplification were modelled: exponential growth phase, slow linear or quadratic growth phase as the magnetic field started to saturate, and the fully saturated phase of the magnetic field. We considered the exponential growth rate of magnetic energy, saturation level of the magnetic energy, the power spectrum of magnetic, and the PDFs of the magnetic and density fields.

Our main conclusion is that SPMHD can successfully reproduce the exponential growth and saturation of an initially weak magnetic field via the small-scale dynamo in magnetized, supersonic turbulence. Our simulation results are summarized as follows.

(i) Both methods exhibited similar qualitative behaviour. The initially weak magnetic field was exponentially amplified at a steady rate over a period of tens of turbulent crossing times, with a slow turnover in magnetic energy corresponding to the slow growth phase. The regions of strongest magnetic field correlated with the high-density regions in the results obtained from both methods. The magnetic energy was amplified by 10 orders of magnitude, saturating when it was 2–4 per cent of the kinetic energy.

(ii) The growth rate of magnetic energy in the FLASH calculations varied only slightly with resolution (5–10 per cent), whereas the PHANTOM calculations nearly doubled the growth rate with each factor of 2 increase in resolution. This was found to be consistent with the resolution scaling of the artificial viscosity and artificial resistivity used to capture shocks and discontinuities in the magnetic field, as these set the level of numerical dissipation, and subsequently, the growth rate.

(iii) PHANTOM is more computationally expensive than FLASH, with the PHANTOM calculations taking approximately $30\times$ more cpu-hours than the FLASH calculations at comparable resolution. The 256^3

PHANTOM calculation required as many cpu-hours as the 512^3 FLASH calculation, consistent with the purely hydrodynamic results of PF10, meaning that adding MHD to SPH adds negligible computational expense.

(iv) In both sets of calculations, the magnetic energy spectrum grew uniformly at all spatial scales during the exponential growth phase. The spectra saturated first at the smallest scale, corresponding to the scale at which energy is injected into the magnetic field, after which there was a phase of slow growth as the magnetic energy spectra slowly saturated at larger scales. This behaviour is consistent with the small-scale dynamo. The magnetic energy spectra in the saturation phase are relatively flat on large scales, peaking around $k \sim 3-5$. The magnetic energy spectra of PHANTOM in the saturation phase contain twice as much magnetic energy at large scales compared to the spectra from FLASH, reflected by the higher mean magnetic energy.

(v) The distribution of magnetic field strengths had similar behaviour in both sets of calculations, both during the exponential growth and saturation phases. During the growth phase, both codes produced a log-normal PDF of B^2 which maintained its width and shape over time, but with the peak increasing to higher field strengths. As the magnetic field approached saturation, the PDF of B^2 deviated from a log-normal distribution. The high-end tail remained fixed during the slow growth phase, but the peak and low-end tail continued increasing leading to a lop-sided distribution. Both the PHANTOM and FLASH results evidenced this behaviour, and agreed on the maximum magnetic field strength and most probable magnetic field strength to within 10 per cent each. FLASH had an extended low-end tail, resulting from SPMHD being adaptive in resolution with density.

(vi) The density PDF was examined during the growth phase before the magnetic field became dynamically important, and during the saturation phase when the magnetic field was strongest. Both codes yielded density PDFs which were log-normal, with possible suggestions that the low-end tail of the distribution was reduced in the saturation phase. The density PDFs of PHANTOM extended further to high densities, whereas the density PDFs of FLASH extended further to low densities. This is a consequence of the density adaptive resolution of SPH.

ACKNOWLEDGEMENTS

We thank the anonymous referee for comments which have improved the quality of this paper. TST is supported by a CITA Postdoctoral Research Fellowship, and was supported by Endeavour IPRS and APA postgraduate research scholarships during which this work was completed. DJP is supported by ARC Future Fellowship FT1130100034, and acknowledges funding provided by the ARC's Discovery Projects (grant no. DP130102078). CF acknowledges funding provided by the Australian Research Council's Discovery Projects (grants DP130102078 and DP150104329). This research was undertaken with the assistance of resources provided at the Multi-modal Australian ScienceS Imaging and Visualization Environment (MASSIVE) through the National Computational Merit Allocation Scheme supported by the Australian Government. We gratefully acknowledge the Jülich Supercomputing Centre (grant hhd20), the Leibniz Rechenzentrum, and the Gauss Centre for Supercomputing (grants pr32lo, pr48pi, and GCS Large-scale project 10391), the Partnership for Advanced Computing in Europe (PRACE grant pr89mu), and the Australian National Computing Infrastructure (grant ek9). Figs 2 and 3 were created using the interactive SPH visualization tool SPLASH (Price 2007).

REFERENCES

- André P. et al., 2010, *A&A*, 518, L102
- Artymowicz P., Lubow S. H., 1994, *ApJ*, 421, 651
- Bate M. R., Tricco T. S., Price D. J., 2014, *MNRAS*, 437, 77
- Berger M. J., Colella P., 1989, *J. Comput. Phys.*, 82, 64
- Bhat P., Subramanian K., 2013, *MNRAS*, 429, 2469
- Børve S., Omang M., Trulsen J., 2001, *ApJ*, 561, 82
- Bourke T. L., Myers P. C., Robinson G., Hyland A. R., 2001, *ApJ*, 554, 916
- Bovino S., Schleicher D. R. G., Schober J., 2013, *New J. Phys.*, 15, 013055
- Brandenburg A., 2010, *MNRAS*, 401, 347
- Brandenburg A., Subramanian K., 2005, *Phys. Rep.*, 417, 1
- Brandenburg A., Jennings R. L., Nordlund Å., Rieutord M., Stein R. F., Tuominen I., 1996, *J. Fluid Mech.*, 306, 325
- Brandenburg A., Sokoloff D., Subramanian K., 2012, *Space Sci. Rev.*, 169, 123
- Cho J., Vishniac E. T., 2000, *ApJ*, 538, 217
- Cho J., Vishniac E. T., Beresnyak A., Lazarian A., Ryu D., 2009, *ApJ*, 693, 1449
- Collins D. C., Kritsuk A. G., Padoan P., Li H., Xu H., Ustyugov S. D., Norman M. L., 2012, *ApJ*, 750, 13
- Courant R., Isaacson E., Rees M., 1952, *Commun. Pure Appl. Math.*, 5, 243
- Crutcher R. M., 1999, *ApJ*, 520, 706
- Crutcher R. M., 2012, *ARA&A*, 50, 29
- Crutcher R. M., Wandelt B., Heiles C., Falgarone E., Troland T. H., 2010, *ApJ*, 725, 466
- Dedner A., Kemm F., Kröner D., Munz C.-D., Schnitzer T., Wesenberg M., 2002, *J. Comput. Phys.*, 175, 645
- Dubey A. et al., 2008, in Pogorelov N. V., Audit E., Zank G. P., eds, *ASP Conf. Ser. Vol. 385, Numerical Modeling of Space Plasma Flows*. Astron. Soc. Pac., San Francisco, p. 145
- Elmegreen B. G., Scalo J., 2004, *ARA&A*, 42, 211
- Eswaran V., Pope S. B., 1988, *Comput. Fluids*, 16, 257
- Federrath C., 2013, *MNRAS*, 436, 1245
- Federrath C., 2015, *MNRAS*, 450, 4035
- Federrath C., 2016, *MNRAS*, 457, 375
- Federrath C., Banerjee S., 2015, *MNRAS*, 448, 3297
- Federrath C., Klessen R. S., 2012, *ApJ*, 761, 156
- Federrath C., Klessen R. S., 2013, *ApJ*, 763, 51
- Federrath C., Klessen R. S., Schmidt W., 2008, *ApJ*, 688, L79
- Federrath C., Roman-Duval J., Klessen R. S., Schmidt W., Mac Low M.-M., 2010, *A&A*, 512, A81
- Federrath C., Chabrier G., Schober J., Banerjee R., Klessen R. S., Schleicher D. R. G., 2011, *Phys. Rev. Lett.*, 107, 114504
- Federrath C., Schober J., Bovino S., Schleicher D. R. G., 2014, *ApJ*, 797, L19
- Fromang S., Papaloizou J., Lesur G., Heinemann T., 2007, *A&A*, 476, 1123
- Fryxell B. et al., 2000, *ApJS*, 131, 273
- Giurchidis P., Konstandin L., Whitworth A. P., Klessen R. S., 2014, *ApJ*, 781, 91
- Goldreich P., Sridhar S., 1995, *ApJ*, 438, 763
- Hacar A., Kainulainen J., Tafalla M., Beuther H., Alves J., 2016, *A&A*, 587, A97
- Hartmann L., 2002, *ApJ*, 578, 914
- Hatchell J., Richer J. S., Fuller G. A., Qualtrough C. J., Ladd E. F., Chandler C. J., 2005, *A&A*, 440, 151
- Haugen N. E., Brandenburg A., Dobler W., 2004, *Phys. Rev. E*, 70, 016308
- Heiles C., Troland T. H., 2005, *ApJ*, 624, 773
- Hennebelle P., Falgarone E., 2012, *A&AR*, 20, 55
- Kainulainen J., Hacar A., Alves J., Beuther H., Bouy H., Tafalla M., 2016, *A&A*, 586, A27
- Kitsionas S. et al., 2009, *A&A*, 508, 541
- Klessen R. S., 2000, *ApJ*, 535, 869
- Konstandin L., Giurchidis P., Federrath C., Klessen R. S., 2012, *ApJ*, 761, 149
- Kowal G., Lazarian A., Beresnyak A., 2007, *ApJ*, 658, 423
- Kritsuk A. G., Norman M. L., Wagner R., 2011a, *ApJ*, 727, L20
- Kritsuk A. G. et al., 2011b, *ApJ*, 737, 13
- Larson R. B., 1981, *MNRAS*, 194, 809
- Lemaster M. N., Stone J. M., 2008, *ApJ*, 682, L97
- Lesaffre P., Balbus S. A., 2007, *MNRAS*, 381, 319
- Lewis B. T., Bate M. R., Price D. J., 2015, *MNRAS*, 451, 288
- Li Y., Klessen R. S., Mac Low M.-M., 2003, *ApJ*, 592, 975
- Lodato G., Price D. J., 2010, *MNRAS*, 405, 1212
- Lunttila T., Padoan P., Juvela M., Nordlund Å., 2009, *ApJ*, 702, L37
- McKee C. F., Ostriker E. C., 2007, *ARA&A*, 45, 565
- Mac Low M.-M., Klessen R. S., 2004, *Rev. Modern Phys.*, 76, 125
- Marder B., 1987, *J. Comput. Phys.*, 68, 48
- Maron J., Cowley S., McWilliams J., 2004, *ApJ*, 603, 569
- Meru F., Bate M. R., 2012, *MNRAS*, 427, 2022
- Molina F. Z., Glover S. C. O., Federrath C., Klessen R. S., 2012, *MNRAS*, 423, 2680
- Monaghan J. J., 1989, *J. Comput. Phys.*, 82, 1
- Monaghan J. J., 1997, *J. Comput. Phys.*, 136, 298
- Monaghan J. J., 2005, *Rep. Progress Phys.*, 68, 1703
- Monaghan J. J., Gingold R. A., 1983, *J. Comput. Phys.*, 52, 374
- Morris J. P., Monaghan J. J., 1997, *J. Comput. Phys.*, 136, 41
- Murray J. R., 1996, *MNRAS*, 279, 402
- Nakamura F., Li Z.-Y., 2008, *ApJ*, 687, 354
- Nolan C. A., Federrath C., Sutherland R. S., 2015, *MNRAS*, 451, 1380
- Nordlund Å. K., Padoan P., 1999, in Franco J., Carraminana A., eds, *Interstellar Turbulence*. Cambridge Univ. Press, Cambridge, p. 218
- Padoan P., Nordlund Å., 2011, *ApJ*, 730, 40
- Padoan P., Nordlund Å., Jones B. J. T., 1997, *MNRAS*, 288, 145
- Padoan P., Federrath C., Chabrier G., Evans N. J., II, Johnstone D., Jørgensen J. K., McKee C. F., Nordlund Å., 2014, in Beuther H., Klessen R. S., Dullemond C. P., Henning T., eds, *Protostars and Planets VI*. University of Arizona Press, Tucson, p. 77
- Pan L., Scannapieco E., 2010, *ApJ*, 721, 1765
- Papoulis A., 1984, *Probability, Random Variables and Stochastic Processes*. McGraw-Hill, New York
- Passot T., Vázquez-Semadeni E., 1998, *Phys. Rev. E*, 58, 4501
- Peretto N. et al., 2012, *A&A*, 541, A63
- Powell K. G., 1994, *Approximate Riemann Solver for Magnetohydrodynamics (that works in more than one dimension)*, Technical report
- Powell K. G., Roe P. L., Linde T. J., Gombosi T. I., De Zeeuw D. L., 1999, *J. Comput. Phys.*, 154, 284
- Price D. J., 2007, *Publ. Astron. Soc. Aust.*, 24, 159
- Price D. J., 2012, *J. Comput. Phys.*, 231, 759
- Price D. J., Bate M. R., 2007, *MNRAS*, 377, 77
- Price D. J., Bate M. R., 2008, *MNRAS*, 385, 1820
- Price D. J., Bate M. R., 2009, *MNRAS*, 398, 33
- Price D. J., Federrath C., 2010, *MNRAS*, 406, 1659 (PF10)
- Price D. J., Monaghan J. J., 2004a, *MNRAS*, 348, 123
- Price D. J., Monaghan J. J., 2004b, *MNRAS*, 348, 139
- Price D. J., Monaghan J. J., 2005, *MNRAS*, 364, 384
- Price D. J., Monaghan J. J., 2007, *MNRAS*, 374, 1347
- Price D. J., Federrath C., Brunt C. M., 2011, *ApJ*, 727, L21
- Price D. J., Tricco T. S., Bate M. R., 2012, *MNRAS*, 423, L45
- Robertson B. E., Kravtsov A. V., Gnedin N. Y., Abel T., Rudd D. H., 2010, *MNRAS*, 401, 2463
- Rosswog S., Price D., 2007, *MNRAS*, 379, 915
- Saitoh T. R., Makino J., 2009, *ApJ*, 697, L99
- Schekochihin A. A., Cowley S. C., Hammett G. W., Maron J. L., McWilliams J. C., 2002, *New J. Phys.*, 4, 84
- Schekochihin A. A., Cowley S. C., Maron J. L., McWilliams J. C., 2004a, *Phys. Rev. Lett.*, 92, 054502
- Schekochihin A. A., Cowley S. C., Maron J. L., McWilliams J. C., 2004b, *Phys. Rev. Lett.*, 92, 064501
- Schekochihin A. A., Cowley S. C., Taylor S. F., Maron J. L., McWilliams J. C., 2004c, *ApJ*, 612, 276
- Schleicher D. R. G., Schober J., Federrath C., Bovino S., Schmidt W., 2013, *New J. Phys.*, 15, 023017
- Schmidt W., Federrath C., Hupp M., Kern S., Niemeyer J. C., 2009, *A&A*, 494, 127

- Schober J., Schleicher D., Federrath C., Klessen R., Banerjee R., 2012a, Phys. Rev. E, 85, 026303
- Schober J., Schleicher D., Bovino S., Klessen R. S., 2012b, Phys. Rev. E, 86, 066412
- Schober J., Schleicher D. R. G., Federrath C., Bovino S., Klessen R. S., 2015, Phys. Rev. E, 92, 023010
- Sridhar S., Goldreich P., 1994, ApJ, 432, 612
- Tasker E. J., Brunino R., Mitchell N. L., Michielsen D., Hopton S., Pearce F. R., Bryan G. L., Theuns T., 2008, MNRAS, 390, 1267
- Tricco T. S., 2015, PhD thesis, School of Mathematical Sciences, Faculty of Science, Monash University
- Tricco T. S., Price D. J., 2012, J. Comput. Phys., 231, 7214
- Tricco T. S., Price D. J., 2013, MNRAS, 436, 2810
- Troland T. H., Crutcher R. M., 2008, ApJ, 680, 457
- Vazquez-Semadeni E., 1994, ApJ, 423, 681
- Waagan K., Federrath C., Klingenberg C., 2011, J. Comput. Phys., 230, 3331
- Wurster J., Price D. J., Bate M. R., 2016, MNRAS, 457, 1037

APPENDIX A: INTERPOLATING PARTICLE DATA TO A GRID

The power spectra of kinetic and magnetic energy of the PHANTOM calculations are computed by interpolating the particle data to a grid using an SPH kernel weighted summation over neighbouring particles. We have investigated whether using mass weighted or volume weighted interpolation changes the results. Furthermore, we have tested grids of varying resolution to find the optimal grid resolution to properly represent the magnetic field.

The volume weighted interpolation of a quantity A (in this case, the magnetic field \mathbf{B}) may be computed according to

$$\mathbf{B}(\mathbf{r}) = \frac{\sum_b \frac{m_b}{\rho_b} \mathbf{B}_b W(|\mathbf{r} - \mathbf{r}_b|, h_b)}{\sum_c \frac{m_c}{\rho_c} W(|\mathbf{r} - \mathbf{r}_c|, h_c)}. \quad (\text{A1})$$

The denominator is the normalization condition. A mass weighted interpolation may be computed as

$$\mathbf{B}(\mathbf{r}) = \frac{\sum_b m_b \mathbf{B}_b W(|\mathbf{r} - \mathbf{r}_b|, h_b)}{\sum_c m_c W(|\mathbf{r} - \mathbf{r}_c|, h_c)}. \quad (\text{A2})$$

Fig. A1 shows the kinetic and magnetic energy spectra for the 256^3 PHANTOM calculation computed from a 512^3 grid using volume weighted and mass weighted interpolations, respectively. The spectra between the two interpolation methods are nearly indistinguishable, differing from each other by less than 1 per cent at all k and deviating only near the resolution scale. We conclude that

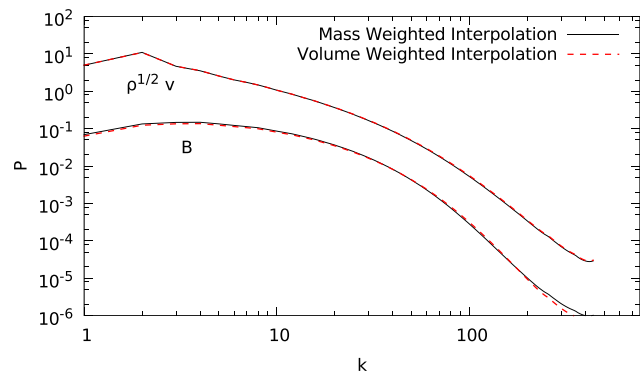


Figure A1. Time averaged kinetic ($\rho^{1/2}v$) and magnetic (B) energy spectra of the 256^3 particle PHANTOM calculation interpolated to a 512^3 grid using mass weighted and volume weighted interpolation. Both approaches yield the same result.

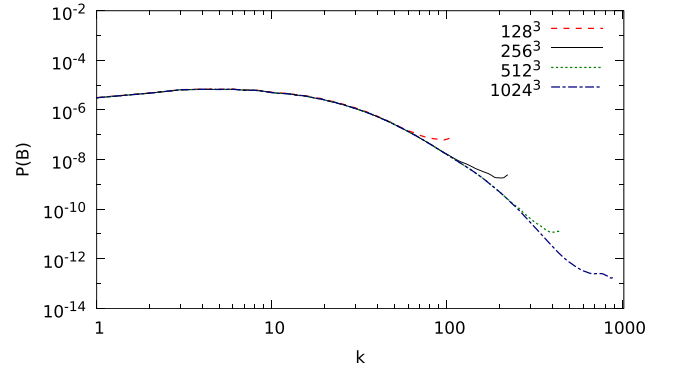


Figure A2. Conversion of a 128^3 particle PHANTOM snapshot to grids of resolutions from 128^3 to 1024^3 grid points. Each resolution agrees well on the large-scale structure, but captures more of the small-scale structure as the resolution is increased. We find that the 256^3 resolution grid sufficiently captures the total magnetic energy, therefore, we choose grids with double the number of grid points as particles for our analysis.

either approach is acceptable, and in this work we have used the mass weighted interpolation.

The smoothing length in our calculations can decrease by up to $8\times$ in the highest density regions, therefore, we have tested the effect of different grid resolutions on the magnetic spectra. Fig. A2 shows magnetic energy spectra from a 128^3 particle PHANTOM calculation interpolated to grids with resolutions of 128^3 – 1024^3 . Our results show that the large-scale structure ($k < 50$) is nearly identical at all grid resolutions, with the spectra differing on the order of 0.1 per cent at each k -band. The only difference is that the spectra extend to higher k as the resolution is increased. We find that the magnetic energy contained on the 128^3 grid differs by 1 per cent of the energy contained on the particles, while the 256^3 grid resolution differs by only 0.1 per cent. Higher resolutions only minimally change the energy content of the magnetic field. Our conclusion is that a grid with double the resolution of the PHANTOM calculation is sufficient for computing the magnetic energy spectrum accurately.

APPENDIX B: EFFECTIVE MAGNETIC PRANDTL NUMBERS IN GRID AND PARTICLE METHODS

B1 Prandtl numbers in Eulerian schemes

The primary source of numerical dissipation in Eulerian schemes is from the discretization of advection terms. Consider a simple example of the contents of one grid cell advecting into an adjacent grid cell. If only a partial amount is transferred into the adjacent cell, then the contents must be reconstructed from the flux across the boundary. This approximation introduces diffusion due to its truncation error (e.g. Robertson et al. 2010). The diffusion term in the first-order upwind scheme of Courant, Isaacson & Rees (1952), for example, scales according to $\propto v \Delta x (1 - |C|)$, where $C = v \Delta t / \Delta x$ is the Courant number. Higher order methods will change the scaling of the diffusion, but in all schemes it depends upon the resolution, time step size, and fluid velocity.

Quantifying the effective numerical dissipation may be done by comparing simulations against analytic solutions. Lesaffre & Balbus (2007) compared the analytic solution of a linear mode of the magnetorotational instability (MRI) to shearing box simulations in order to calibrate their version of ZEUS3D. They varied the size of the time step and investigated resolutions from 32^3 to 128^3 ,

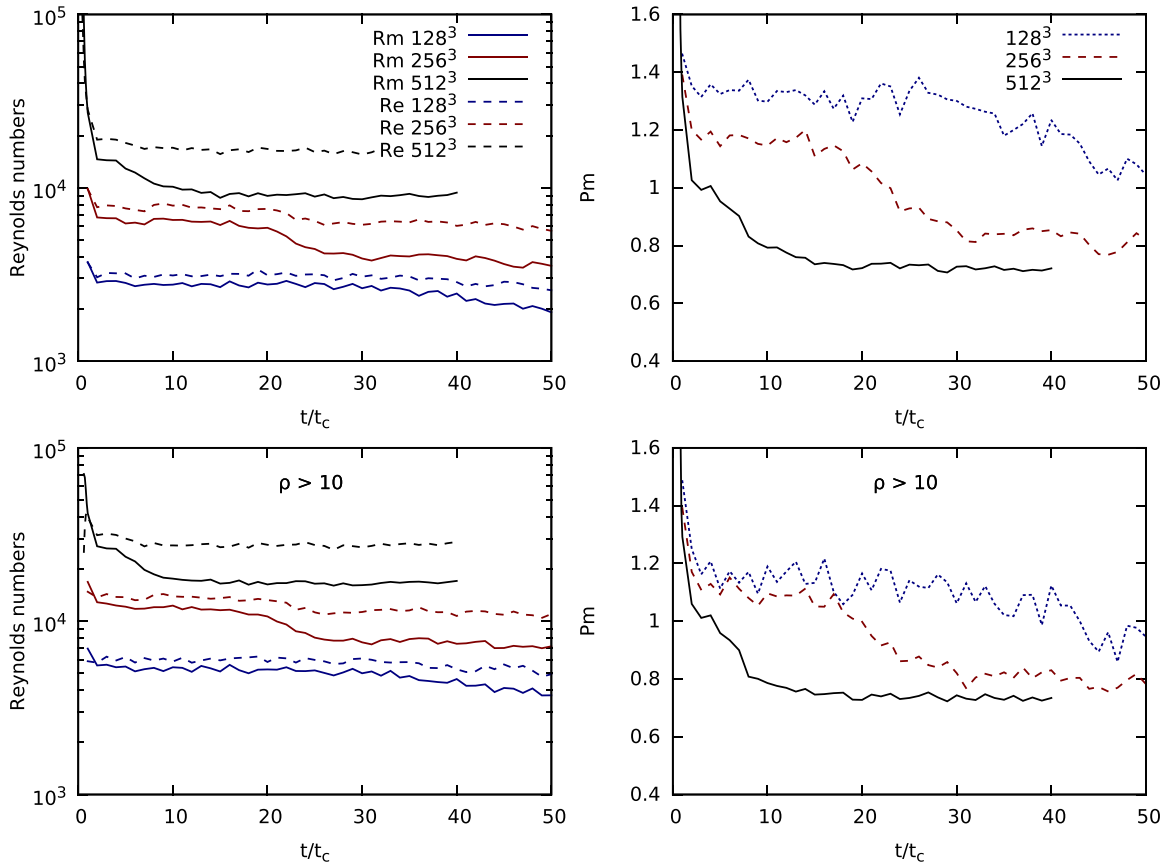


Figure B1. The kinetic and magnetic Reynolds numbers (left-hand plots) and Prandtl numbers (right-hand plots) for PHANTOM. The top row shows the averaged numbers for particles which have $\nabla \cdot \mathbf{v} < 0$, while the bottom row is averaged for regions where $\rho > 10\rho_0$. The higher density regions have approximately double the kinetic and magnetic Reynolds numbers. The drop in Reynolds and Prandtl numbers over time is due to the fast MHD wave speed increasing in the signal velocity of the artificial dissipation terms. The Prandtl numbers are about unity, though decrease with resolution.

determining that the total numerical dissipation (viscous and resistive) scaled linearly with time and quadratically with resolution. They found the magnetic Prandtl number to be approximately 2 (though in the context of this comparison, these simulations are for subsonic flows). In a similar manner, Fromang et al. (2007) performed simulations of the MRI with and without physical viscous and resistive dissipation terms. They found that the results of their ideal MHD simulations (dissipation is purely numerical) corresponded to $\text{Pm} \approx 2$, though cautioned that this depends upon the nature of the flow.

The effective Prandtl number for the version of FLASH used in this paper was calibrated by Federrath et al. (2011). Using simulations of the small-scale dynamo amplification of a magnetic field, they compared results from ideal MHD simulations to simulations employing a fixed dissipation (at varying resolution). They found that $\text{Pm} \approx 2$ for flows of Mach numbers 0.4 and 2. Thus, it is expected that the FLASH calculations in our comparison will have a similar Prandtl number.

B2 Prandtl numbers in SPMHD

In SPMHD, the equations of motion are derived from the discretized Lagrangian (Price & Monaghan 2004b; Price 2012). Advection is computed exactly. Hence, the only sources of numerical dissipation are from the explicit sources of artificial viscosity and resistivity, which can be used to estimate the Reynolds and Prandtl numbers.

Artificial viscosity and resistivity in SPMHD are discretizations of physical dissipation terms, but with diffusion parameters that depend on resolution. Artymowicz & Lubow (1994) and Murray (1996) analytically derived the amount of corresponding physical dissipation from the Monaghan & Gingold (1983) form of artificial viscosity (see also Monaghan 2005; Lodato & Price 2010). The artificial viscosity acts as both a shear and bulk viscosity. In these calculations, we use the Monaghan (1997) form of artificial viscosity, which is similar except for the absence of a factor $h/|r_{ab}|$. Meru & Bate (2012) calculated the amount of viscosity this adds in the continuum limit, and have shown that for the Monaghan (1997) form of viscosity, it is approximately 18 per cent stronger for the α term. Using this approach, they also derived the coefficients for the β_{AV} term in the signal velocity. The shear viscosity in our simulations is estimated according to

$$v_{\text{AV}} = \frac{62}{525} \alpha v_{\text{sig}} h + \frac{9}{35\pi} \beta_{\text{AV}} |\nabla \cdot \mathbf{v}| h^2, \quad (\text{B1})$$

where

$$v_{\text{sig}} = \sqrt{c_s^2 + v_A^2}. \quad (\text{B2})$$

The bulk viscosity will be $5/3 \times$ this value (Lodato & Price 2010).

These coefficients are twice the values quoted by Meru & Bate (2012). Their work is derived in the context of a Keplerian accretion disc, in which they safely assume that half the particles inside a particle volume are approaching while the other half are receding.

It is standard in SPH to apply artificial viscosity only to approaching particles. In this paper, we calculate Reynolds numbers for particles where $\nabla \cdot \mathbf{v} < 0$, and use the full value of the coefficient as it is expected that inside a shock, nearly all particles will be approaching. In order to compare Reynolds numbers with *FLASH*, we compute the Reynolds numbers using only the shear viscosity, but note that the artificial viscosity will introduce a bulk viscosity which would be dynamically relevant for supersonic flows. Including this term would reduce the estimate of the Reynolds number and lead to larger Pm values, but it is not clear how bulk viscosity would affect the small-scale dynamo.

The corresponding physical dissipation from the artificial resistivity can be calculated in a similar manner (Price 2012). Artificial resistivity corresponds to a physical resistivity given by

$$\eta_{\text{AR}} \approx \frac{1}{2} \alpha_{\text{B}} v_{\text{sig}} h. \quad (\text{B3})$$

We note, as concluded in Tricco & Price (2013), that the β_{AV} term in the artificial viscosity is not required for artificial resistivity. It is added to artificial viscosity to prevent particle interpenetration

in high Mach number shocks, and otherwise leads to unnecessary dissipation if added to artificial resistivity.

Since the dissipation terms use the local signal velocity, and our simulations use switches to dynamically adjust the values of α and α_{B} for each particle, v_{AV} and η_{AR} are calculated per particle. In Fig. B1, we show the average kinetic Reynolds, magnetic Reynolds, and magnetic Prandtl numbers on the particles for our simulations. We find that the mean Prandtl number in these set of SPMHD calculations is approximately unity. The Prandtl number decreases with resolution, a consequence of the quadratic scaling of the β_{AV} term, which is present in the artificial viscosity but not artificial resistivity. The Prandtl number also decreases with time. This results from the signal velocity scaling behaviour, as the dissipation from the α term increases as the magnetic field is amplified (v_{A} increasing). The β_{AV} term is unaffected by this. For high-density regions ($\rho > 10$), we note that the Reynolds numbers are increased by approximately a factor of 2, directly corresponding to the reduction in h .

This paper has been typeset from a $\text{\TeX}/\text{\LaTeX}$ file prepared by the author.